

# Reconstruction of depth profiles of thermal conductivity of case hardened steels using a three-dimensional photothermal technique

Hong Qu,<sup>1</sup> Chinhua Wang,<sup>1,a)</sup> XinXin Guo,<sup>2</sup> and Andreas Mandelis<sup>2</sup>

<sup>1</sup>Key Laboratory of Modern Optical Technologies of Jiangsu Province, Institute of Modern Optical Technologies, Soochow University, Suzhou, Jiangsu 215006, People's Republic of China

<sup>2</sup>Department of Mechanical and Industrial Engineering, Center for Advanced Diffusion-Wave Technologies (CADIFT), University of Toronto, Toronto M5S 3G8, Canada

(Received 23 July 2008; accepted 16 October 2008; published online 8 December 2008)

A method of retrieving thermophysical depth profiles of continuously inhomogeneous materials is presented both theoretically and experimentally using laser infrared photothermal radiometry. This method represents the three-dimensional (3D) extension of earlier one-dimensional thermal-wave inverse-problem techniques for reconstructing inhomogeneous thermal-conductivity or diffusivity depth profiles. A 3D theoretical model suitable for characterizing solids with arbitrary continuously varying thermophysical property depth profiles and finite (collimated or focused) laser beam spotsize is developed. A numerical fitting algorithm to retrieve the thermophysical profile was demonstrated with three case hardened steel samples. The reconstructed thermal conductivity depth profiles were found to be well anticorrelated with microhardness profiles obtained with the conventional indenter method. © 2008 American Institute of Physics. [DOI: 10.1063/1.3035831]

## I. INTRODUCTION

Laser infrared photothermal radiometry (PTR) has proven to be a powerful tool for the thermophysical characterization and nondestructive evaluation (NDE) of various materials. The principle of PTR is based on the detection of changes in thermal radiation emission from a material surface as a result of the absorption of an intensity-modulated laser beam. One of the most important capabilities of photothermal techniques (PTs) is the nondestructive characterization of thermophysical properties and defects or subsurface features on the order of a few micrometers to millimeters in depth in composite or inhomogeneous materials through thermal-diffusion-length probing by scanning the modulation frequency of the incident laser power. This feature of the PTs has been used very effectively in the evaluation of discretely layered structures, in which two, three, or more layers or thin film coatings are characterized nondestructively.<sup>1-3</sup> In recent years, PTs have expanded to applications to inhomogeneous materials with continuously varied properties. One example is the NDE of the case depth profile of hardened steels. Various independent research groups reported a well-established anticorrelation between thermal diffusivity or thermal conductivity and microhardness.<sup>4-7</sup> The surface structure of a case hardened sample is an inhomogeneous layer with continuously varying thermophysical parameters from the surface to the unhardened core (bulk) of the sample. To retrieve the depth profile of the thermophysical parameters of the inhomogeneous hardened layer, several “inverse” algorithms have been developed and demonstrated.<sup>8-11</sup> In those studies, a one-dimensional (1D) measurement scheme was employed in which the incident laser beam was assumed to be large enough compared with the thermal diffusion length in the

frequency range of interest, so as to simplify the mathematical algorithm by assuming a 1D treatment. Under three-dimensional (3D) (finite laser beam) conditions, Fabbri and Cernuschi<sup>12</sup> studied the thermal-wave interferometric effects of finite beam sizes in discretely layered solids.

The work presented in this paper is motivated by the increasing reduction in PTs to industrial practice, in which finite incident beam size [to maintain an acceptable signal-to-noise ratio (SNR) and to address issues of accessibility to surfaces shaded by component overlayers, such as in gear tooth inspection] and thermoelectrically cooled detectors (compared with the conventional liquid nitrogen cooled detectors) are favored as the sole alternatives. Therefore, in this paper, we propose a new method suitable for characterizing materials with arbitrary thermophysical depth profiles, photothermally probed with arbitrary incident laser beam sizes. A 3D thermal-wave theoretical model was developed and a numerical fitting algorithm to retrieve the thermal conductivity depth profile was demonstrated with three case hardened steel samples. Experiments were performed with thermoelectrically cooled detectors and were validated using microhardness depth profiles obtained with a conventional mechanical indenter.

## II. THEORETICAL MODEL

A case hardened steel sample can be considered as an inhomogeneous system, which contains an inhomogeneous (i.e., hardened) layer and a homogeneous substrate (i.e., unhardened bulk). The physical parameters in the inhomogeneous layer, such as the microhardness, thermal conductivity, and thermal diffusivity, are a function of depth and may have different distributions along the depth direction. A typical configuration is shown in Fig. 1. To quantitatively evaluate the inhomogeneous system, a grid multilayer thermal-wave propagation model is developed to simplify the complexity

<sup>a)</sup>Author to whom the correspondence should be addressed. Electronic mail: chinhua.wang@suda.edu.cn.

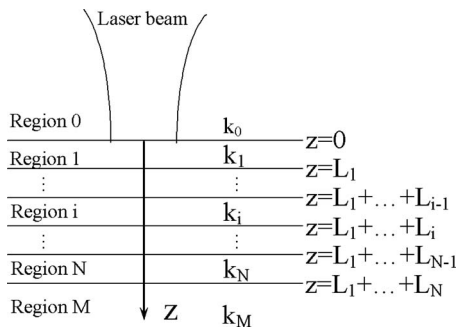


FIG. 1. A 3D configuration cross section of an inhomogeneous multilayer system. Region 0 is air, regions 1 to  $N$  represent the sublayers of the inhomogeneous layer, and region  $M$  is the homogeneous substrate (semi-infinite).

of the inhomogeneity. The inhomogeneous layer is divided into  $N$  layers thin enough that each layer can be considered thermophysically homogeneous. When the number of layers is appropriately chosen (large enough), the multilayer model can be a good approximation of a continuous model. In Fig. 1 the system contains a total of  $(N+2)$  layers, where region 0 is the ambient gas (air) and region  $M$  is the substrate layer (assumed to be semi-infinite). Region 1 to  $N$  includes the divided sublayers of the inhomogeneous layer, in which region  $N$  is the last sublayer and next to substrate region  $M$ . The thermal conductivity, thermal diffusivity, and thickness of region  $i$  are denoted by  $k_i$ ,  $\alpha_i$ , and  $L_i$ , respectively. A Gaussian laser beam, intensity-modulated at frequency  $f$ , with radius  $a$  and power  $P$ , impinges normally on the sample along the  $z$ -axis. The temperature increase in region  $i$  satisfies the thermal-wave equation

$$\nabla^2 T_i(r, z, \omega) - \sigma_i^2 T_i(r, z, \omega) = 0 \quad (i = 0, 1, 2, \dots, M), \quad (1)$$

where  $\sigma_i = (1+j)\sqrt{\omega/2\alpha_i}$  is the complex thermal wavenumber and  $\alpha_i = k_i/\rho_i c_i$  is the thermal diffusivity of layer  $i$ . The boundary conditions at  $z = L_1 + L_2 + \dots + L_i$ ,  $1 \leq i \leq M$ , at the interface between virtual slices or regions  $(i)$  and  $(i+1)$ , and at  $z=0$  are, respectively,

$$T_i(r, z, \omega) = T_{i+1}(r, z, \omega), \quad (2)$$

$$k_i \frac{\partial T_i(r, z, \omega)}{\partial z} = k_{i+1} \frac{\partial T_{i+1}(r, z, \omega)}{\partial z},$$

$$T_0(r, z=0, \omega) = T_1(r, z=0, \omega), \quad (3)$$

$$k_0 \frac{\partial T_0(r, z=0, \omega)}{\partial z} - k_1 \frac{\partial T_1(r, z=0, \omega)}{\partial z} = Q_S(0),$$

where  $Q_S(0) = \eta_S(0)A_S(1-R_1)P/(\pi a^2 e^{-r^2/a^2})$ .  $R_1$  and  $A_S$  represent the surface reflection and absorption coefficient of the sample, respectively.  $a$  is the radius of the incident laser beam. By using the Hankel transformation, the thermal-wave field at the sample surface in Hankel space can be obtained as<sup>13</sup>

$$\begin{aligned} \tilde{T}_1(\lambda, z=0, \omega) \\ = A_1 + B_1 = \frac{Q_S(0)}{k_0 \delta_0 (1 + b_{1,0})} \frac{1 + g_1 e^{-2\delta_1 L_1}}{1 + \gamma_{1,0} g_1 e^{-2\delta_1 L_1}} e^{-\lambda^2 a^2/4}, \end{aligned} \quad (4)$$

where

$$g_i = \frac{1 - b_{i+1,i} p_{i+1}}{1 + b_{i+1,i} p_{i+1}}, \quad p_{i+1} = \frac{1 - g_{i+1} e^{-2\delta_{i+1} L_{i+1}}}{1 + g_{i+1} e^{-2\delta_{i+1} L_{i+1}}},$$

$$b_{i+1,i} = \frac{k_{i+1} \delta_{i+1}}{k_i \delta_i}, \quad \delta_i^2 = \lambda^2 + \sigma_i^2, \quad (5)$$

$$\gamma_{1,0} = \frac{1 - b_{1,0}}{1 + b_{1,0}}, \quad g_N = \frac{1 - b_{M,N}}{1 + b_{M,N}}.$$

Equation (5) gives recurrence relations for  $g_i$  and  $p_i$ . In the computation,  $g_{i+1}$  is calculated first, then  $p_{i+1}$  is calculated using  $g_{i+1}$ .  $g_i$  is then obtained, followed by  $p_i$ ,  $g_{i-1}$ , ..., and so on. Upon repeated application, the coefficient  $g_1$  appearing in Eq. (4) can be computed. Using the inverse Hankel transform of Eq. (4), the thermal-wave field at the sample surface can be obtained. This is the quantity directly measured by PTR,

$$\begin{aligned} T_1(r, z=0, \omega) \\ = \int_0^\infty \tilde{T}_1(\lambda, z=0, \omega) J_0(\lambda r) \lambda d\lambda \\ = \int_0^\infty \frac{Q_S(0)}{k_0 \delta_0 (1 + b_{1,0})} \frac{1 + g_1 e^{-2\delta_1 L_1}}{1 + \gamma_{1,0} g_1 e^{-2\delta_1 L_1}} \\ \times e^{-\lambda^2 a^2/4} J_0(\lambda r) \lambda d\lambda. \end{aligned} \quad (6)$$

### III. THEORETICAL SIMULATIONS AND DISCUSSION

To quantitatively characterize the case depth profile of the inhomogeneous thermophysical parameters in case hardened samples, a proper mathematical description of the thermal conductivity/diffusivity depth profile is needed in the form of a convenient analytical formula (ansatz). The assumed depth profile ansatz must meet several requirements corresponding to general features of case hardened steel depth profiles encountered in our samples: (1) the thermophysical parameters should be a monotonic function of depth  $z$  with the possibility to increase or decrease; (2) the thermophysical profile must saturate at a determined depth to conform with the unhardened bulk of the sample; and (3) the number of parameters involved in the ansatz should be as small as possible to minimize the complexity of the computational best fit and fitting time. Equation (7) gives the assumed formula<sup>8</sup>

$$k(z) = k_0 \left( \frac{1 + \Delta e^{-qz}}{1 + \Delta} \right)^2 \quad \text{and} \quad \Delta = \frac{1 - \sqrt{k_0/k_{L_0}}}{\sqrt{k_{L_0}/k_0} - e^{-qL_0}}, \quad (7)$$

where  $k_0$  and  $k_{L_0}$  represent the values of the thermal conductivity at the two boundary surfaces  $z=0$  and  $L_0$ , respectively.  $L_0$  is the total thickness of the inhomogeneous surface layer. Figure 2 shows that Eq. (7) is capable of describing all pos-

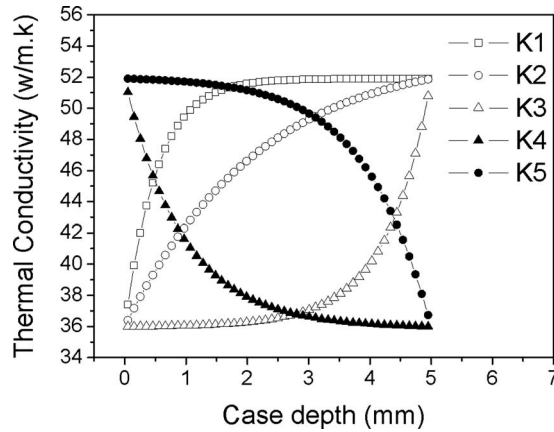


FIG. 2. Various thermal conductivity depth profiles obtained using the  $k(z)$  ansatz [Eq. (7)]. The parameters used are as follows: curve K1:  $k_0 = 36$  W/m K,  $k_{L_0} = 51.9$  W/m K,  $q = 2 \times 10^3$  mm $^{-1}$ , and  $L_0 = 5$  mm; curve K2:  $k_0 = 36$  W/m K,  $k_{L_0} = 51.9$  W/m K,  $q = 0.5 \times 10^3$  mm $^{-1}$ , and  $L_0 = 5$  mm; curve K3:  $k_0 = 36$  W/m K,  $k_{L_0} = 51.9$  W/m K,  $q = -2 \times 10^3$  mm $^{-1}$ , and  $L_0 = 5$  mm; curve K4:  $k_0 = 51.9$  W/m K,  $k_{L_0} = 36$  W/m K,  $q = 1 \times 10^3$  mm $^{-1}$ , and  $L_0 = 5$  mm; and curve K5:  $k_0 = 51.9$  W/m K,  $k_{L_0} = 36$  W/m K,  $q = -1 \times 10^3$  mm $^{-1}$ , and  $L_0 = 5$  mm.

sible monotonic curves with depth. It can be seen that Eq. (7) is adequate for expressing arbitrary monotonic profiles if parameters are properly chosen. The profile of the thermal conductivity is determined by the combination of  $k_0$ ,  $k_{L_0}$ ,  $q$ , and  $L_0$ .

In what follows, we will discuss the effects of several material and experimental parameters on the behavior of the PTR signal. In all simulations the unhardened substrate is assumed to be AISI 9310 steel, the thermophysical parameters of which are  $k = 36.049$  W/m K,  $\rho = 7750$  g/cm $^3$ , and  $c = 493.93$  J/kg °C.<sup>14</sup> It should be mentioned that in the simulation, the thermal diffusivity and the thermal conductivity of each layer are related by a constant product  $c\rho$ . This can be justified by the experimental fact that the thermal diffusivity and the thermal conductivity are strongly correlated for hardened steel products and the  $c\rho$  product is almost independent of hardness.<sup>6</sup> For simplicity and clarity, the thermal-wave field was calculated at  $r = 0$  (i.e., the center of the laser spot), which corresponds to the arrangement that the photothermal signal is optimized or maximized through mechanical adjustment to ensure the coincidence of the laser heating spot and the measurement spot in the experiment. In the simulation, an appropriate number of the sublayers  $N$  should be considered in order to ensure sufficient computational accuracy and depth profile fidelity for the continuously graded samples.  $N = 31$  is used in the simulation.

### A. Effect of beam size $a$

In these simulations we assume the parameters of the case hardened layer to be as follows:  $k_0 = 20$  W/m K,  $k_{L_0} = 36.0489$  W/m K,  $q = 2529$  mm $^{-1}$ , and  $L_0 = 2.45$  mm. The depth profile of the thermal conductivity of the hardened layer is shown in Fig. 3. Figure 4 shows the amplitude and phase of a thermophysically inhomogeneous system, the frequency response of each quantity normalized by that generated with the same beam size from a semi-infinite unhardened homogeneous AISI 9310 steel. It is seen from Fig. 4

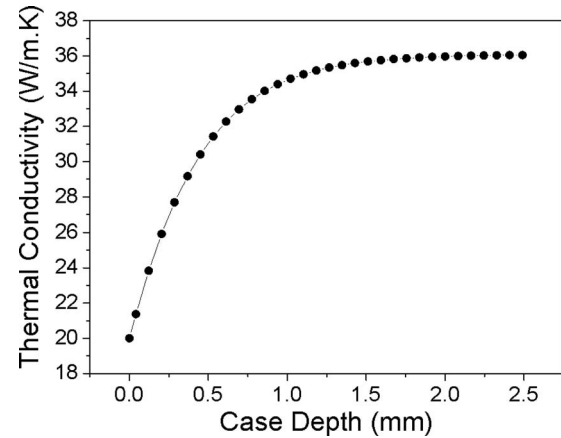


FIG. 3. Thermal conductivity depth profile of the hardened layer. Parameters used are  $k_0 = 20$  W/m K,  $k_{L_0} = 36.0489$  W/m K,  $q = 2529$  mm $^{-1}$ , and  $L_0 = 2.45$  mm.

that the amplitude and phase are very sensitive to beam size. With increasing beam size from 0.01 mm (3D limit) to 100 mm (1D limit), the magnitude and frequency positions of the normalized phase minimum decrease and shift to lower frequencies. This can be understood when consideration is given to the relative sizes of the thermal diffusion length and

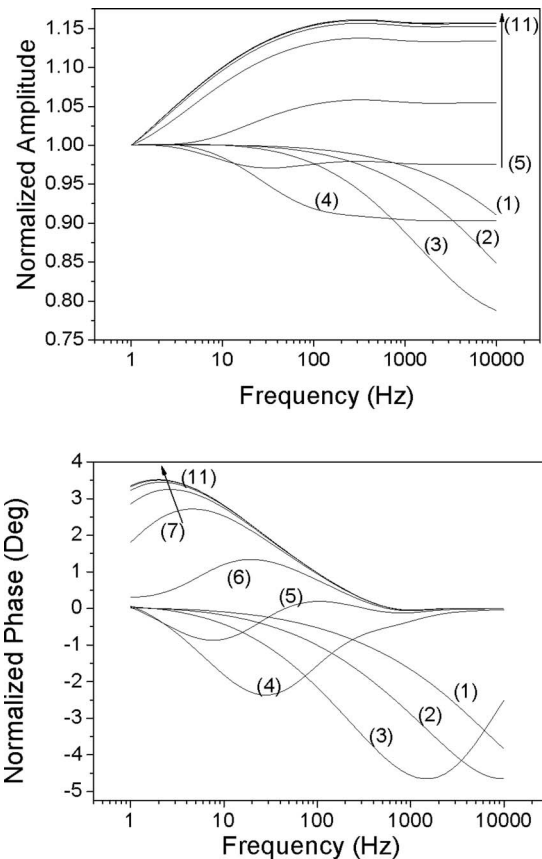


FIG. 4. Amplitude and phase of a steel with inhomogeneous thermal conductivity simulating a case-hardened AISI 9310 normalized by the corresponding homogeneous AISI 9310 semi-infinite steel sample using several beam sizes  $a$  (mm): (1) 0.01, (2) 0.02, (3) 0.05, (4) 0.5, (5) 1.0, (6) 2.0, (7) 5.0, (8) 10, (9) 20, (10) 40, and (11) 100. Other parameters of the hardened layer used are  $k_0 = 20$  W/m K,  $k_{L_0} = 36.0489$  W/m K,  $q = 2529$  mm $^{-1}$ , and  $L_0 = 2.45$  mm.

beam size. In the approximate 1D limit (large beam size) the diffusion length of the generated thermal wave matches the beam size at very low frequencies, contributing an interference phase maximum in the 1–10 Hz range. Since the case hardened layer thermal conductivity is smaller than that of the bulk, the relative amplitude is larger than unity until the beam size leads to strictly 1D regime and the relative amplitude converges to unity (and the relative phase to zero) as shown in Fig. 4. With decreasing beam sizes the diffusion length-to-beam size equality is attained at higher frequencies as witnessed by the phase minimum shifts in Fig. 4(b). The additional (sideways) degrees of freedom in thermal-wave power conducted away from the laser source represent a loss to the local thermal-wave field, resulting in lower amplitudes compared with the semi-infinite unhardened steel. This is manifested by the  $<1$  normalized amplitudes in Fig. 4(a). When the beam size is larger than 1 mm, the minimum shown in the case of small beam sizes disappears and a maximum emerges and shifts toward lower frequencies. This minimum-to-maximum inversion occurs because at this limit the standing thermal wave within the hardened region clearly reaches the effective interface with the better conducting substrate/bulk, which makes the back-propagating contribution to the interference pattern sensitive to the (negative) sign of the interface coupling (depletion) coefficient<sup>15</sup> to yield conductive loss. This is opposite to the 3D interference condition involving the diffusion length versus beam size equality discussed above. In that case, the confinement of the thermal-wave power within the illuminated area amounts to an interference pattern of conductive gain within a layer of very similar thermophysical properties surrounding the illuminated spot. This leads to an interferometric phase extremum opposite to that generated by material interfaces. The phase maximum eventually saturates when beam size becomes larger than 20 mm. From Fig. 4 it is clear that the largest phase maxima can be obtained with either a very small beam size ( $<0.05$  mm; strongest interference stemming from the condition of thermal-diffusion-length and beam-size equality attained at high frequencies) or a very large beam size ( $>5$  mm; strongest interface depletion transport effect attained at very low frequencies). The minima appearing at high frequencies ( $>1000$  Hz) are subject to experimental distortion and noise resulting from surface roughness.<sup>11</sup> On the other hand, low-frequency PTR signals with large beam sizes suffer from low SNR. Therefore, in practice, the selection of beam size is a trade-off between measurement sensitivity and SNR and is usually set at  $\sim 1$  mm

### B. Effect of case depth $L_0$

In this simulation, thermophysical parameters of the hardened layer are assumed to be  $k_0=30$  W/m K,  $k_{L_0}=36.0489$  W/m K,  $q=1952.7$  mm<sup>-1</sup>, and beam size  $a=1$  mm. The effective case depth  $L_0$  is defined as the thickness where the thermal conductivity begins to saturate, i.e., where the value of the conductivity is equal to that of bulk. Figure 5 shows the assumed depth profile of the thermal conductivity of the hardened layer and Fig. 6 shows the ef-

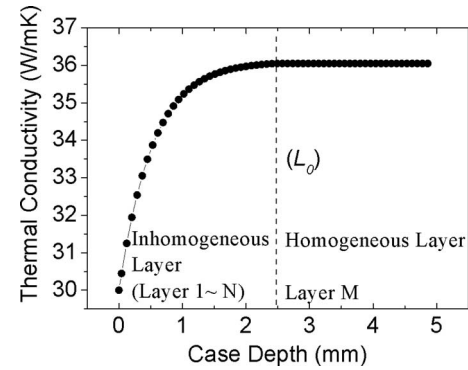


FIG. 5. Thermal conductivity depth profile of the case hardened layer.  $L_0$  is the thickness at which the thermal conductivity begins to saturate. Parameters used are  $k_0=30$  W/m K,  $k_{L_0}=36.0489$  W/m K,  $q=1952.7$  mm<sup>-1</sup>, and beam size  $a=1$  mm.

fect of the value of  $L_0$  on the behavior of the PTR signal. It is seen that both amplitude and phase are very sensitive to changes in effective thickness  $L_0$ . At small values of  $L_0$  the thermal-wave confinement within the surface layer of low thermal conductivity compared with the bulk exhibits only 1D thermal-wave interference patterns at high frequencies as expected from a thin confinement layer, leading to amplitude ratios  $>1$  and positive phase antinodes (maxima). Increasing  $L_0$  shifts the interference antinode pattern to lower frequencies with simultaneous decrease in the normalized amplitude, as the confinement layer grows and thermal-wave power shifts to larger depths and sideways conductive heat losses characteristic of 3D thermal-wave behavior. The inversion of

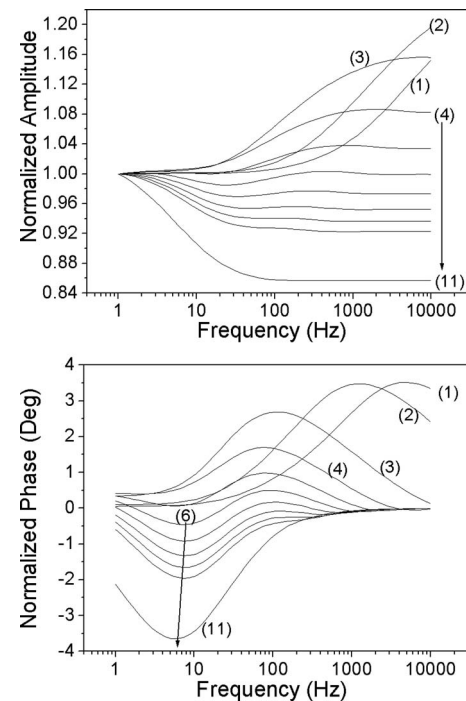


FIG. 6. Amplitude and phase of a steel with inhomogeneous thermal conductivity simulating a case-hardened AISI 9310 steel normalized by the corresponding homogeneous AISI 9310 steel sample with different effective case depths  $L_0$  (mm): (1) 0.05, (2) 0.1, (3) 0.5, (4) 1.0, (5) 1.5, (6) 2.0, (7) 2.5, (8) 3.0, (9) 3.5, (10) 4.0, and (11) 10.0. Other parameters of the hardened layer are  $k_0=30$  W/m K,  $k_{L_0}=36.0489$  W/m K,  $q=1952.7$  mm<sup>-1</sup>, and beam size  $a=1$  mm.

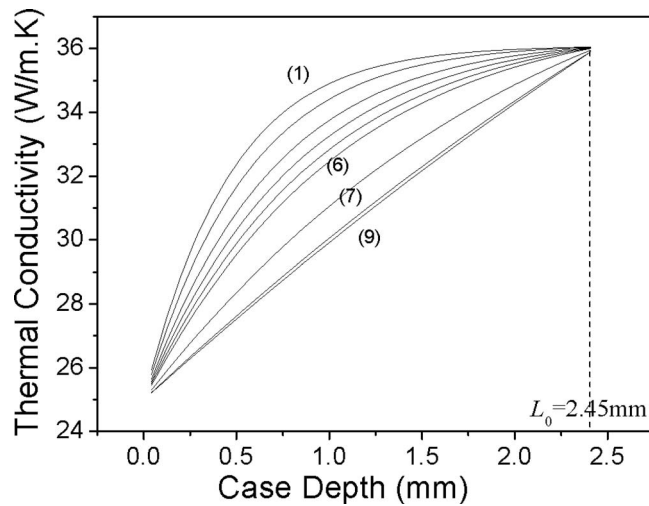


FIG. 7. Thermal conductivity depth profiles of the case hardened layer with various values of the exponent  $q$  representing the curvature of the profile ( $q$  in  $\text{mm}^{-1}$ ): (1) 2312.5, (2) 1933.3, (3) 1553.2, (4) 1324.6, (5) 1152.3, (6) 1012.5, (7) 546.4, (8) 214.6, and (9) 200.

the phase extrema to minima occurs when the (effective constructive) interference between laser beam size (1 mm) and thermal diffusion length is established at approximately 6–8 Hz [also see Fig. 4(b), the minimum in curve 5]. Since the laser beam size remains fixed, the condition for this type of interference does not change with increasing  $L_0$  and as a result the phase minimum remains at the same frequency. Nevertheless, the thicker surface layer is one of increased sideways conductive heat loss, which shifts the phase lag farther away from the surface and decreases the relative amplitude, as shown at the low-frequency limit of Fig. 6.

### C. Effect of curvature $q$ of the thermal conductivity depth profile

For fixed thickness of the hardened layer, different curvatures of the depth profile may exhibit different PTR signal behaviors. The curvature of the depth profile can be changed though the exponential factor  $q$ . Figure 7 shows several depth profiles of the thermal conductivity of the hardened layer with different values of  $q$ . Figure 8 shows the effect of  $q$  on the behavior of the PTR signal. The magnitude of change in both amplitude and phase increases with decreasing  $q$ , i.e., with decreasing curvature of the thermal conductivity depth profile  $k(z)$ . This is as expected since the effective thickness of the low-conductivity hardened layer decreases with increasing  $k(z)$  curvature, which results in increased thermal-wave depletion into the more highly conductive bulk.<sup>15</sup> This leads to delocalization of the thermal-wave centroid away from the surface,<sup>13</sup> lower relative amplitudes, and more pronounced phase interference extrema (minima) with the (fixed) position of the minimum at approximately 6–8 Hz, consistent with Fig. 4(b) for laser spot-size  $a=1$  mm.

### D. Effect of surface thermal conductivity $k_0$

Figure 9 shows the effect of the surface conductivity  $k_0$  on the behavior of the PTR signal. Given that  $L_0$

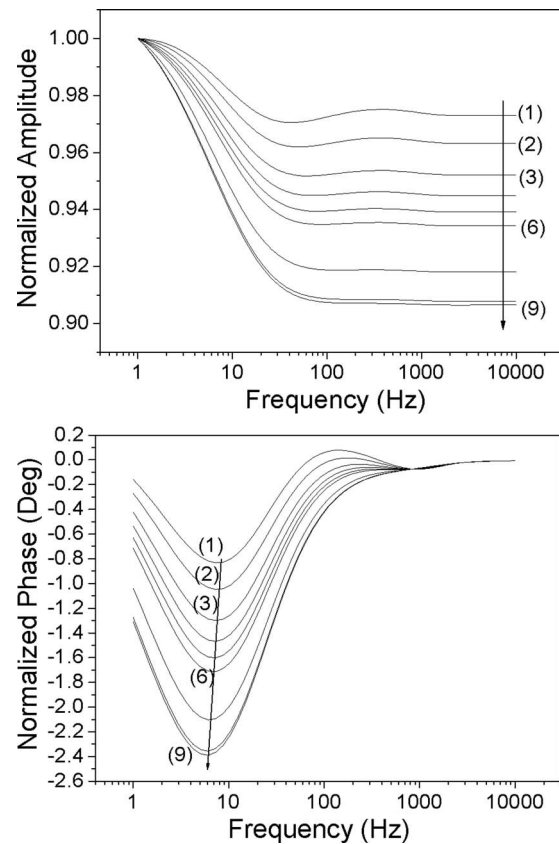


FIG. 8. Amplitudes and phases of inhomogeneous hardened AISI 9310 steel structures with different curvatures  $q$  of depth profile normalized by the corresponding homogeneous semi-infinite AISI 9310 steel sample. The  $q$  values (1)–(9) correspond to those shown in Fig. 7. Other parameters of the hardened layer are  $k_0=25$  W/m K,  $k_{L_0}=36.0489$  W/m K, beam size  $a=1$  mm, and  $L_0=2.45$  mm.

$=2.45$  mm and beam size  $a=1$  mm in this simulation, the gentle normalized amplitude maximum ( $<1$ ) at approximately 200–300 Hz and phase minimum at 6–8 Hz are expected from and are consistent with Fig. 6, a result of 3D sideways conductive thermal-wave losses and the superposed (effective destructive) interference within the hardened surface layer on account of the fact that the substrate steel is a better conductor than the hardened overlayer. With increasing  $k_0$  from 10 to 35 W/m K, the contrast of physical properties between the inhomogeneous layer and the substrate decreases and the extrema in amplitude and phase gradually diminish, as expected.

## IV. EXPERIMENTAL RESULTS

To demonstrate the developed mathematical algorithm, PTR experiments were performed using carburized AISI 9310 steel (0.08%–0.13% C, 0.45%–0.65% Mn, and 0.15%–0.3% Si) with three different case hardened depths, labeled A1, A2, and A3, respectively. The samples were cylindrical plates with a 30 mm diameter and a 9.5 mm thickness. The PTR measurements were performed on the flat surface. The thermophysical parameters of the unhardened AISI 9310 steel are  $k=36.049$  W/m K,  $\rho=7750$  g/cm<sup>3</sup>, and  $c=493.93$  J/kg °C.<sup>14</sup> The samples were subjected to a standard industrial carburizing hardening process, which resulted

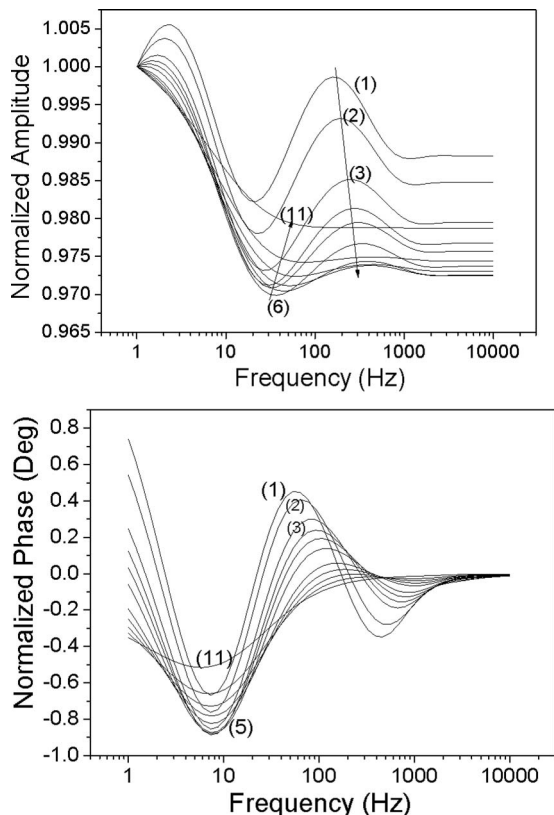


FIG. 9. Amplitude and phase of a steel with inhomogeneous thermal conductivity simulating a case-hardened AISI 9310 steel normalized by the corresponding homogeneous AISI 9310 steel sample with various values of surface conductivity  $k_0$  (W/m K): (1) 10, (2) 12, (3) 16, (4) 18, (5) 20, (6) 22, (7) 26, (8) 28, (9) 29, (10) 32, and (11) 35. The remaining parameters used in the plot are  $k_{L_0}=36.0489$  W/mK,  $L_0=2.45$  mm,  $q=2312.5$  mm<sup>-1</sup>, and laser beam size  $a=1$  mm.

in a hardened case depth ranging from 0.5 to 2 mm depending on the conditions of the hardening process. The experimental PTR system is shown in Fig. 10. The thermal-wave source was a high-power (~20 W) 808 nm semiconductor diode laser. The laser was modulated by a periodic current driver, the frequency of which was controlled by the computer and also served as the lock-in reference, with range from 1 to 10<sup>4</sup> Hz. In the experiment, a Gaussian beam with a radius of ~1 mm [defined as the half-width at the (1/e) intensity] was used. A thermoelectrically-cooled HgCdZnTe (MCZT) detector was used in the measurements, replacing

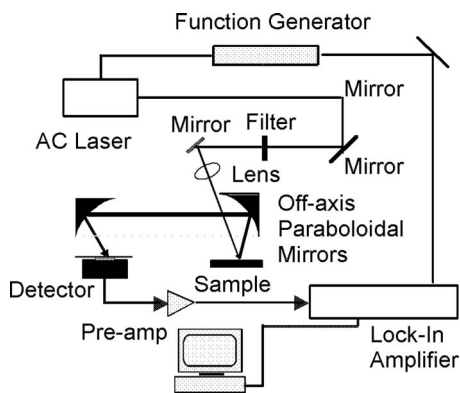


FIG. 10. The PTR experimental system.

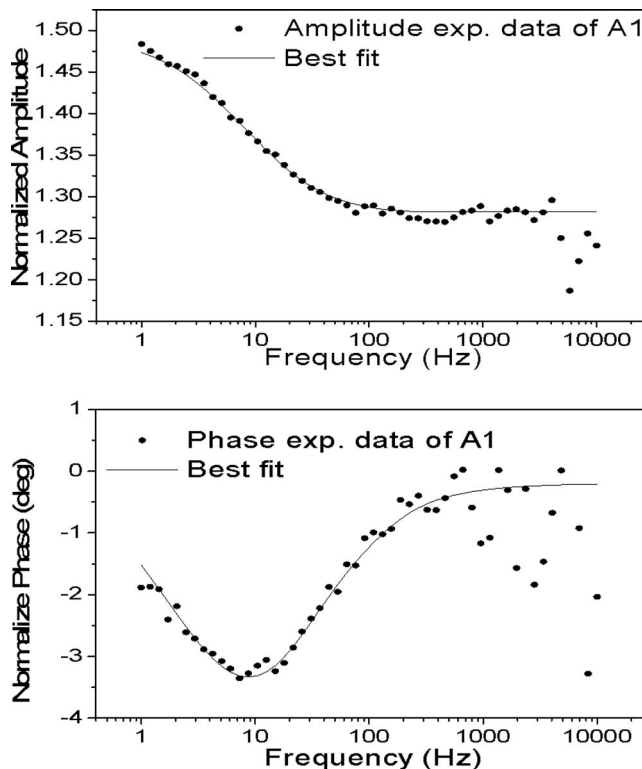


FIG. 11. Comparison of the normalized PTR amplitude and phase between best-fitted results and experimental data for sample A1. Best-fitted parameters are given in Table I.

the conventional liquid-nitrogen-cooled HgCdTe (MCT) detector. The advantage of the MCZT detector is the elimination of the frequent liquid nitrogen filling and refilling, which poses danger to operators and would require untenable special LN2 housing facilities in industrial environments where, for example, steel hardness inspection is routinely performed. The trade-off is the relatively low detectability of the thermoelectrically cooled detectors when compared with the conventional liquid-nitrogen cooled MCT detector (at least six times lower), resulting in lower SNR. Figures 11–13 show the experimental frequency scans and the corresponding best-fit results using the algorithm described above for samples A1, A2, and A3, respectively. The best-fitted thermal conductivity profiles of the three samples are shown in Fig. 14. In the best-fit process, four parameters were set as the fitting variables:  $k_0$ ,  $L_0$ ,  $q$ , and beam size  $a$ . Other parameters used were as follows:  $k_{L_0}=k_M=36.0489$  W/m K and  $\alpha_M = k_M/\rho C = 9.4173 \times 10^{-6}$  m<sup>2</sup>/s for AISI 9310 steel. It is seen from Figs. 11–13 that all fits are reasonably good in view of the fact that the SNR of the experimental data is limited especially at high frequencies. The fitted profiles of the thermal conductivity in Fig. 14 show that sample A1 has a smaller conductivity gradient toward bulk saturation than A2 and A3, which implies that sample A1 has the thickest case depth among the three samples. Sample A2 lies in the middle and sample A3 has the shallowest case depth. The detailed best-fit results for samples A1, A2, and A3 are given in Table I. The best-fitted beam sizes are approximately ~0.8 mm, which is close to the experimental measurement. The fitted value of  $L_0$  represents the thickness at which the thermal

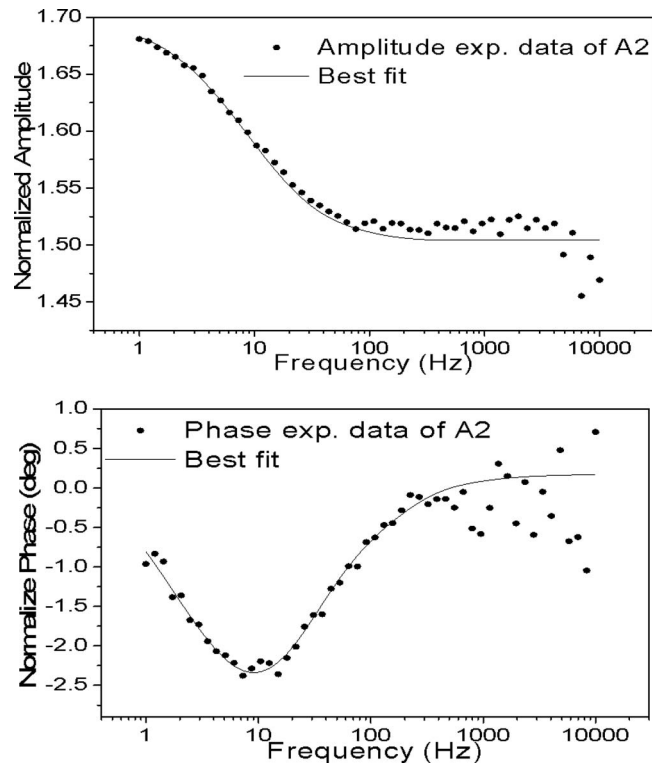


FIG. 12. Comparison of the normalized PTR amplitude and phase between best-fitted results and experimental data for sample A2. Best-fitted parameters are given in Table I.

conductivity of the inhomogeneous layer saturates to the thermal conductivity of the unhardened bulk, which corresponds to the total thickness of the virtual slice stack from 1 to  $N$ , as described in the theoretical model.

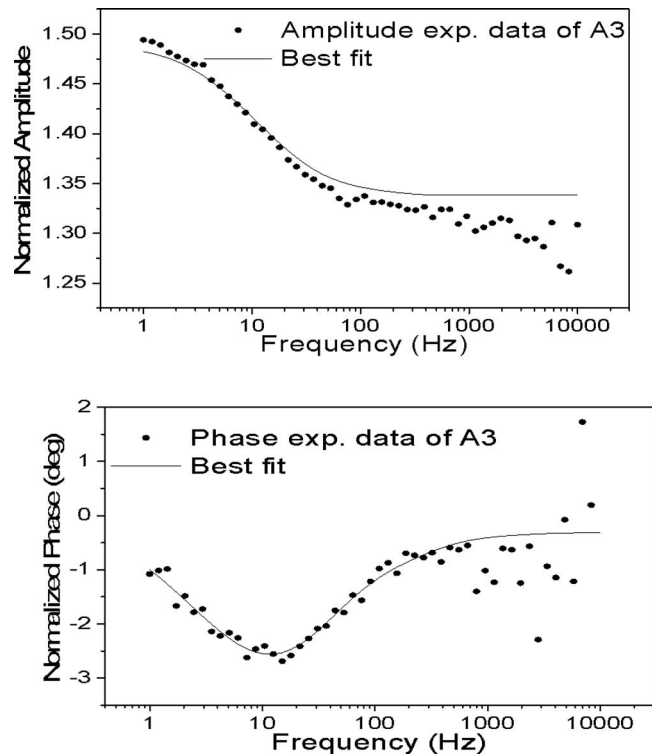


FIG. 13. Comparison of the normalized PTR amplitude and phase between best-fitted results and experimental data for sample A3. Best-fitted parameters are given in Table I.

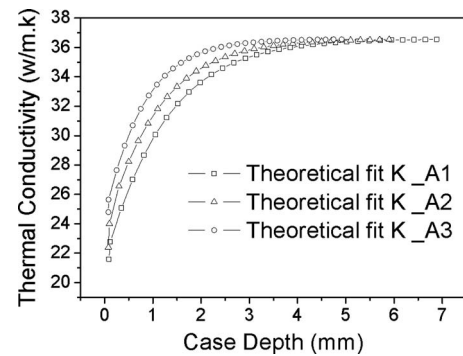


FIG. 14. Reconstructed thermal conductivity depth profiles of samples A1, A2, and A3 obtained through best fitting the experimental data to PTR theory [Eqs. (6) and (7)].

It should be mentioned that the relatively low SNR shown in the experimental data, compared with our previous results,<sup>16</sup> is actually the result of substitution of the nitrogen-cooled MCT detector with a thermoelectrically cooled MCZT detector. The purpose of using the MCZT detector is to simulate the measurement sensitivity of the system as it would be used for real-time industrial applications, in which nitrogen cooling is impractical, dangerous, and not favored.

To verify the reconstruction of the case depths, the microhardness depth profiles of the three samples were established using the conventional destructive indenter test. The test results are shown in Fig. 15. The case depths of samples A1, A2, and A3 are approximately 2.45, 1.95, and 1.1 mm, respectively, to the depth where the hardness drops to 440 HV. An anticorrelation between the reconstructed thermal conductivity profiles and microhardness depth profiles is thus found in all three samples. Quantitative correlations can be extracted by defining the fractional change in thermal conductivity and microhardness, respectively, as  $\Delta K = (k_{L_0} - k_0)/k_{L_0}$  and  $\Delta H = (H_0 - H_{L_0})/H_0$ . The calculated fractional changes are listed in Table II. It is seen that the fractional change in the thermal conductivity and the microhardness are in good agreement, which means that the hardness change is well anticorrelated with the thermophysical property change. The polynomial fits of the microhardness depth profiles in Fig. 15 show that the effective case depths are approximately  $L_{A1} = 2.73$  mm,  $L_{A2} = 2.19$  mm, and  $L_{A3} = 1.9$  mm for samples A1, A2, and A3, respectively. These values are very close to those obtained using the PTR reconstruction results, i.e., 2.9, 2.4, and 2.1 mm, respectively, as shown in Fig. 14. Due to the limited number of data points shown in the microhardness measurements, the effective microhardness case depth in Fig. 15 may be larger than shown in that figure especially for samples A2 and A3.

TABLE I. Best-fit results for samples A1, A2, and A3 using PTR theory [Eqs. (6) and (7)].

Sample	$k_0$ (W/m K)	$L_0$ (mm)	$q$ (mm <sup>-1</sup> )
A1	21.1	2.9	842.5
A2	21.6	2.4	978.1
A3	24.2	2.1	1169.9

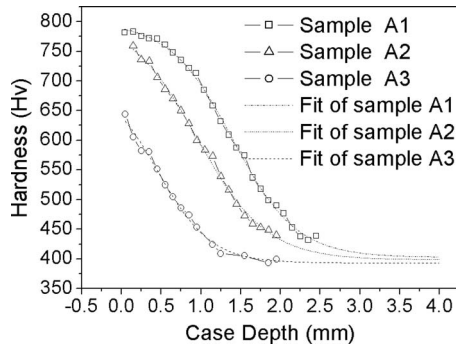


FIG. 15. Microhardness depth profiles of samples A1, A2, and A3 measured by a microhardness indenter and numerical best fits to calculate the case depths.

It is helpful to discuss the uncertainty of the best-fit results shown in Figs. 11–13. In the fitting process, four parameters were set as the fitting variables:  $k_0$ ,  $L_0$ ,  $q$ , and beam size  $a$ . The sensitivity of the best-fitted curve of the normalized phase to each of those four parameters has been analyzed. Figure 16 shows the typical sensitivity of the theoretical fit to parameter  $k_0$  for sample A1. Figure 16(a) shows the best-fitted curve and the theoretically calculated curves with various deviations from the best-fitted value  $k_0$ . It is seen that the calculated curves with  $\pm 5\%$  deviation in  $k_0$  diverge significantly from the best fitted curve and the experimental data, which is obviously unacceptable. Similar detailed examinations have also been performed with respect to parameters  $L_0$ ,  $q$ , and beam size  $a$  and similar sensitivities ( $\pm 5\%$ ) of the normalized phase curve to deviations in these parameters were also found. Therefore, it is believed that the overall best-fit uncertainty is around  $\pm 2\%$ . Figure 16(b) gives the depth profiles of the thermal conductivity calculated with  $\pm 2\%$  deviations in  $k_0$  shown in Fig. 16(a). The diverging curves are very close to the best-fitted curve. It is interesting to see that with the aforementioned deviations in  $k_0$ , the calculated phase at high frequencies (i.e., the large noise region) is actually saturated, which implies insensitivity of the phase value at high frequencies to deviations in fitting parameters. The most sensitive region (most significant feature) for best fitting the experimental results is at low frequencies around 1–100 Hz. A detailed numerical analysis shows that a  $\pm 2\%$  deviation from the best-fitted value in all four parameters, i.e.,  $k_0$ ,  $L_0$ ,  $q$ , and  $a$  will result in an  $\sim \pm 3\%$  deviation in the final reconstructed depth profile of the thermal conductivity (averaged over the whole curve), as shown in Fig. 16(b).

## V. CONCLUSIONS

A new method using PTR data obtained with a finite-size Gaussian laser beam was developed for reconstructing the

TABLE II. Fractional changes in microhardness depth profiles between the surface values and the 440 HV level (Fig. 15 and the corresponding fractional changes in thermal conductivities.

Sample	Fractional change in $k(z)$	Fractional change in microhardness
A1	0.4175	0.438
A2	0.4008	0.4203
A3	0.3620	0.3804

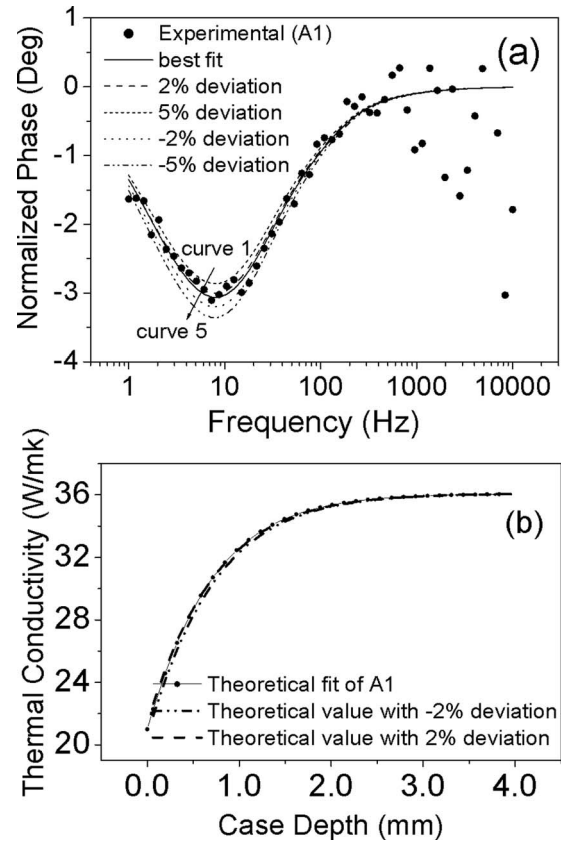


FIG. 16. Uncertainty analysis of the theoretical best fits for sample A1. (a) Sensitivity of the normalized phase with various deviations from the best-fitted value  $k_0$ . Curves 1–5 represent 5%, 2%, 0% (best fitted), -2%, and -5% deviations, respectively. (b) Depth profiles of thermal conductivity with  $\pm 2\%$  deviations in  $k_0$ .

depth profile of the thermal conductivity in inhomogeneous structures. This method represents the 3D extension of earlier 1D thermal-wave inverse-problem techniques for reconstructing inhomogeneous thermal-conductivity or diffusivity depth profiles. The technique was demonstrated with three case hardened AISI 9310 steel samples and exhibited very good agreement between the reconstructed depth profiles of thermal conductivity and microhardness depth profiles.

## ACKNOWLEDGMENTS

The support of AVIO Propulzione Aerospaziale, Turin, Italy, through a contract to A.M. is gratefully acknowledged. This work was supported by a grant from the National Natural Science Foundation of China (Contract No. 60877063) and Scientific Research Foundation for Returned Scholars, Ministry of Education of China.

<sup>1</sup>M. Depriester, P. Hus, S. Delenclos, and A. Sahraoui, *Rev. Sci. Instrum.* **76**, 074902 (2005).

<sup>2</sup>M. Reichling and H. Gronbeck, *J. Appl. Phys.* **75**, 1914 (1994).

<sup>3</sup>B. Li and S. Y. Zhang, *J. Appl. Phys.* **30**, 1447 (1997).

<sup>4</sup>J. Jaarinen and M. Luukkala, *J. Phys. (Paris)* **44**, C503 (1983).

<sup>5</sup>T. T. N. Lan, H. G. Walther, G. Goch, and B. Schmitz, *J. Appl. Phys.* **78**, 4108 (1995).

<sup>6</sup>H. G. Walther, D. Fournier, J. C. Krapez, M. Luukkala, B. Schmitz, C. Sibilia, H. Stamm, and J. Thoen, *Nat. Sci.* **17**, s165 (2001).

<sup>7</sup>D. Fournier, J. P. Roger, A. Bellouati, C. Boue, H. Stamm, and F. Lakestani, *Nat. Sci.* **17**, s158 (2001).

- <sup>8</sup>M. Munidasa, F. Funak, and A. Mandelis, *J. Appl. Phys.* **83**, 3495 (1998).
- <sup>9</sup>T. C. Ma, M. Munidasa, and A. Mandelis, *J. Appl. Phys.* **71**, 6029 (1992).
- <sup>10</sup>L. Nicolaides, A. Mandelis, and C. J. Beingsner, *J. Appl. Phys.* **89**, 7879 (2001).
- <sup>11</sup>L. Nicolaides and A. Mandelis, *J. Appl. Phys.* **90**, 1255 (2001).
- <sup>12</sup>L. Fabbri and F. Cernuschi, *J. Appl. Phys.* **82**, 5305 (1997).
- <sup>13</sup>A. Mandelis, *Diffusion-Wave Fields: Mathematical Methods and Green Functions* (Springer, New York, 2001), Chap. 3.
- <sup>14</sup>SAE 9310, Data on world wide metals and alloys, Alloy Digest Inc., SA-444, 1990.
- <sup>15</sup>A. Mandelis, L. Nicolaides, and Y. Chen, *Phys. Rev. Lett.* **87**, 020801 (2001).
- <sup>16</sup>C. Wang, A. Mandelis, H. Qu, and Z. Chen, *J. Appl. Phys.* **103**, 043510 (2008).